Advanced Composites and Hybrid Materials (2023) 6:103
https://doi.org/10.1007/s42114-023-00681-w

RESEARCH

Synergistic effect of integrating N-functionalized graphene and PEDOT:PSS as hole transporter bilayer for high-performance perovskite solar cells

A. G. Al-Gamal[1,2] · Ahmed Mourtada Elseman[3] · M. Abdel-Shakour[2,4] · T. H. Chowdhury[2] · K. I. Kabel[1] · A. A. Farag[1] · A. M. Rabie[1] · N. E. A. Abd El-Sattar[5] · Naoki Fukata[6,7] · Ashraful Islam[2,7]

Received: 2 December 2022 / Revised: 18 April 2023 / Accepted: 27 April 2023

Abstract
Hole transport layers (HTLs) are one of the most significant elements influencing the performance of perovskite solar cells (PSCs). PEDOT:PSS (= Poly (3,4-ethylenedioxythiophene):poly(styrenesulfonate)) is regarded to be the most conducting polymer to use as an organic HTL for the inverted structure of PSCs. Due to the highly acidic behavior, PEDOT:PSS-based PSCs have shown limited stability. Additionally, the valence band mismatch of the PEDOT:PSS layer with the adjacent perovskite layer often results in low open-circuit voltage (V_{OC}) of the overall PSC. To address these issues, we have incorporated a thin layer of ethylenediamine functionalized graphene (EDA-FG) between the indium tin oxide (ITO) anode and the PEDOT:PSS layer yielding a bilayer HTL. The new bilayer successfully matches the energy valence band at the HTLs/perovskite layer interface. The photoluminescence (PL) confirms that the deposited EDA-FG/PEDOT:PSS quenched the perovskite layer more than PEDOT:PSS. Based on the enhanced electrical and optical properties, a champion PCE of 17.66% was obtained for the respective PSCs. Additionally, the PSCs showed stable photovoltaic behavior up to 500 h.

Keywords Functionalized graphene · PEDOT:PSS · Bilayer · Perovskite solar cell · Stability

1 Introduction

Compared to mesoporous organic–inorganic perovskite solar cells (PSCs), which recorded a power conversion efficiency (PCE) exceeding 25%, the inverted structure of PSCs granted more beneficial properties, including their long-term stability, low hysteresis, and low-temperature processed [1–4]. In typical inverted (p-i-n) PSCs, the light absorber layer, perovskite film, is placed between two chargers' carriers; electron and hole-transporting layers (ETLs and HTLs) [5]. In order to increase the hole collection, several conductive polymers (i.e., PEDOT:PSS with PCE over 20% [6–9], poly (triarylamine) (PTAA) [10–12]) and metal oxides (i.e., NiO_x [13–16], V_2O_5 [17,

A. G. Al-Gamal and A. M. Elseman equally contributed to this work.

✉ Ahmed Mourtada Elseman
amourtada@cmrdi.sci.eg; AhmedMourtada5555@yahoo.com

✉ Ashraful Islam
ISLAM.Ashraful@nims.go.jp

[1] Egyptian Petroleum Research Institute (EPRI), Nasr City, Cairo 11727, Egypt

[2] Photovoltaic Materials Group, Center for Green Research On Energy and Environmental Materials, National Institute for Materials Science (NIMS), 1-2-1 Sengen, Tsukuba, Ibaraki 305-0047, Japan

[3] Electronic & Magnetic Materials Department, Central Metallurgical Research and Development Institute (CMRDI), P.O. Box 87, Helwan, Cairo 11421, Egypt

[4] Chemistry Department, Faculty of Science, Assiut University, Assiut 71516, Egypt

[5] Chemistry Department, Faculty of Science, Ain Shams University, Abbassia, Cairo 11566, Egypt

[6] International Center for Materials Nanoarchitectonics, National Institute for Materials Science, Tsukuba, Ibaraki 305-0044, Japan

[7] Faculty of Pure and Applied Sciences, University of Tsukuba, Tsukuba, Ibaraki 305-8573, Japan

Published online: 18 May 2023

18], CoO_x [19, 20], Cu_2ZnSnS_4 [21], and CuSCN [22, 23]) have been utilized as HTLs too. Particularly PEDOT:PSS was adopted as the most efficient conductive-polymers HTLs in the inverted PSCs; however, its acidic property can influence the perovskite layer in the long run [24, 25].

Graphene (G) and its allotropes were successfully applied as an alternative candidate as HTLs for PEDOT:PSS due to its unique characteristics, such as good stability, optoelectronic property, and long-term stability [26, 27]. Unfortunately, G's work function (WF) is around 4.9 eV, and this value has a severe mismatch with the adjacent perovskite absorber layer. Graphene-based HTLs result in poor surface morphology and a non-homogenous film with low surface coverage [26, 28, 29]. To overcome the defects in both types of HTLs, some reports synergized benefits by combining them as HTLs using two different techniques: intercalation of the G into PEDOT:PSS, while another is forming a bilayer HTL which consists of PEDOT:PSS and one of the graphene allotropes [30, 31]. Intercalation of a layer between HTLs and charges' collector electrodes is a known technique utilized to enhance the PCE of PSCs devices [32, 33]. In the case of graphene derivatives/PEDOT:PSS as bilayer HTL for inverted PSCs (p-i-n structure) with methylammonium lead iodide (MAPI3) as a light-absorber layer, the supreme PCE of 16.89% was achieved with GO-polyethylene glycol (PEG) above PEDOT:PSS [34]. Redondo-Obispo et al. showed an easy low-temperature spin-coating technique for preparing homogenous PEDOT:PSS thin-film doped with graphene oxide (GO). The obtained results showed that the PSCs device based on PEDOT:PSS-doped GO enhanced the electrical conductivity and crystallinity of the perovskite layer without declining the optical transmittance [31]. Feng et al. followed bilayer HTLs techniques by precipitating GO and modified with NH_3 layer on the top of PEDOT:PSS to form a PSCs with configuration (PEDOT:PSS)-GO:NH_3/$CH_3NH_3PbI_{3-x}Cl_x$/PCBM/Bphen/Ag. The obtained results depicted that PSCs based on bilayer HTLs structure can significantly improve the performance and stability of PCE up to 16.11% [30].

Recently, many articles stated that grafting the G surface with multifunctional amines, including but not limited to triethylenetetramine (TETA), diethylenetriamine (DETA), and ethylene diamine (EDA), was achieved using different methods, including spin-coating, dipping, and vapor phase depositions [35]. The amination of the G with nitrogen heterostructures improved its electronics and optical properties. In addition to films, resistance, hole mobility, electrical conductivity, and charges carriers densities, as well as the work function (WF), were significantly improved without impacting the transmittance of the G layer compared to pristine G, which promotes using N-DG as an HTL in the PSCs [36, 37].

Here, we stress the benefits of the HTLs using the bilayer technique. Firstly, a simple solvothermal method synthesized ethylenediamine functionalized graphene (EDA-FG). The synthesized EDA-FG was spun-coated and then dropped on top of the ITO glass. On top of the EDA-FG layer, a thin PEDOT:PSS layer was spin-coated. The fabricated bi-layer HTLs of EDA-FG/PEDOT:PSS with various concentrations of EDA-FG (0.25, 0.5, and 1.0 mg. mL^{-1}) were examined by XRD, SEM, and UV–Vis. The electrical resistances of various deposited HTLs, including EDA-FG, PEDOT:PSS, and bi-layer HTLs structures, were measured by electrochemical impedance spectroscopy (EIS). The performances of different fabricated devices based on EDA-FG, PEDOT:PSS, and bi-layer HTLs are investigated. Among the evaluated HTLs, 0.5 mg. mL^{-1} EDA-FG/PEDOT:PSS-based PSCs showed PCE of 17.39% and long-term stability over 500 h, the highest obtained photovoltaic performance compared with other PSCs devices fabricated by PEDOT:PSS or EDA-FG.

2 Experimental

2.1 Preparation of graphene-ethylenediamine (EDA-FG)

The GO was obtained from graphite powder [38]. The EDA-FG was prepared by a direct solvothermal interaction between the acquired GO and EDA solution in the presence of Li metal and ammonium hydroxide (NH_4OH) as catalysts and nitrogen dopant agents, respectively. The dried GO precipitate was mixed with EDA into the autoclaves to form a physical adsorbed EDA over the GO surface. After forward, the hydrothermal was heated in a muffle at 200 °C—4 h. The reaction finished when the suspension color changed to black color (see Fig. S1a). The EDA-FG residues are washed per 0.1 M HCl to eliminate the excess EDA and Li, subsequently frequently rinsing with ethanol (Eth) and H_2O to remove any impurities. The obtained product EDA-FG was dried overnight under a vacuum at 60 ℃ to eradicate the amines that were physically attached to the G plate's surface, then well-kept-up for more analysis. The photographs of GO and EDA-FG solution taken under 365 nm UV light are shown in Fig. S1b.

2.2 Cell fabrication

An aqueous solution of PEDOT:PSS was first spun onto the ITO substrate before being annealed for 15 min at 150 °C at 1500 and 4000 rpm for 15 and 20 s, respectively. The formation of an interfacial film based on EDA-FG was initialized via 120 µL (0.25, 0.5, and 1 mg mL^{-1} suspendered

in diethyl ether were deposited under PEDOT:PSS with 2000 rpm (25 s) tracked by 4000 rpm for 15 s, and the film was desiccated at 50 °C for 10 min). Fig. S1c in the supplementary information (SI) describes the made-up HTL with a bilayer structure with an optical image for every step. Then, $MAPbI_3$ precursor perovskite solution (110 µL) containing CH_3NH_3I (343 mg) and PbI_2 (998 mg) well dissolved in 1.8 mL of 5:1 (v/v) DMF/DMSO was cast onto the resultant bilayer HTLs by spinning at 1000 rpm and 5000 rpm for 12 s and 30 s, respectively. Anti-solvent (chlorobenzene, 100 µL) was dropped on the top of the perovskite (PSK) layer, and the spinning increased to 5000 rpm after 5 s, starting the solvent eviction, and the PSK film was annealed for 15 min at 120 °C. Next, the ETL layer was formed by spin-coated PCBM/chlorobenzene (20 mg/mL) perovskite layer for 30 s at 1000 rpm. To inhibit the corrosion of perovskite by Ag anode, 140 µL of BCP saturated solution was deposited on top of the PCBM layer at rotation for 30 s/6000 rpm. The production of the devices was finished by physical vapor deposition of Ag as an electrode (70 nm) (0.09 cm^2 active area). The steps of PSCs device fabrications with bilayer structure are illustrated in Fig. S1d.

3 Results and discussion

The effect of crosslinking between EDA-FG and PEDOT:PSS is optimized and highlighted in this work. Through a newly created bond between N-functionalized and PEDOT:PSS, the sulfonamide bond is proved by FT-IR. The possible crosslinking between EDA-FG and PEDOT:PSS is discussed via FTIR spectra which are presented in detail in the SI (Fig. 1c). A schematic of a possible sulfonamide bond via a PSCs device is shown in Fig. 1a. It can be seen that the linkage led to rearrangement between PEDOT:PSS intermolecular and thus enhanced its film crystallinity, which pushes in the direction of depositing better PSK crystals. Crosslinking occurs by every plate terminated -NH_2 of EDA-FG that can bond to free sulphonic groups of polystyrene sulphonic acid (PSS). Taking into account the fact that PEDOT:PSS consists of Poly(3,4-ethylene dioxythiophene) blended with polystyrene sulfonate and poly (styrene sulfonic acid) [39].

To realize EDA-FG's role with different concentrations in the PSK layer enhancement, XRD of various deposited PSK over a single layer and bilayer's HTLs with other structures were observed (Fig. 1b). It can be seen that the sharp intensity at 14.11°, 28.05°, 31.61°, and 34.89° are related to the (110), (220), (310), and (312) diffraction planes of the PSK layers. In the case of single-layer HTLs, EDA-FG/PSK, these peaks are roughly shifted to higher diffraction angles by 0.2 than PEDOT:PSS, which explains that the G in its reduced form can influence the preferential growth of large PSK crystals than PEDOT:PSS [26]. The PSK layer deposited on the pristine PEDOT:PSS is reasonably rough due to random grains growth and superposition with each other [30]. Fortunately, inserting the EDA-FG layer at the bottom of PEDOT:PSS reduces the roughness and wettability of the PEDOT:PSS surface, while the PEDOT:PSS surface improvement reaches its maximum at 0.5 EDA-FG mg mL^{-1} concentration. Typically, by increasing EDA-FG concentration 2θ angle shifted to the lower diffraction angle, which is primarily responsible for a drop in grain size or nonuniform strain [40]. Despite in our case, the size of perovskite crystals is substantially greater than the pristine PEDOT:PSS. As a result, the shift in the diffraction peak should be attributed to inhomogeneous strain in the perovskite crystal, which may be connected to the epitaxial growth of the perovskite on the HTL bilayer structure [41].

On the other hand, adding graphene derivatives like GO under PEDOT:PSS decreased its wettability [42]. In our case, following to contact angle measurement, its value decreased from 12.8° (± 1.3) to 6.9° (± 0.9) for only PEDOT:PSS and 0.5 EDA-FG/PEDOT:PSS as shown in Fig. 1e and f, respectively. This reverse phenomenon may be due to the decline of the sulfonic group responsible for PEDOT:PSS wetting due to its interaction with the amine group present in EDA-FG and the formation of the sulfonamide bond.

The morphological surface enhancement of PEDOT:PSS, in turn, is reflected in the crystallinity of PSK films, where the intensities of the peaks ratios of $I_{(110)}/I_{(220)}$ impressively increased from 1.59 to 1.97 for pristine PEDOT:PSS and 0.5 EDA-FG/PEDOT:PSS, respectively. The EDA-FG may enhance the PEDOT:PSS surface through crosslinking effect by forming the sulfonamide bond confirmed previously by FTIR analysis (Fig. 1c). This cross-linking has occurred through the terminated -NH_2, which bonded to free sulphonic groups [39]. This linkage led to rearrangement between PEDOT:PSS intermolecular and thus enhanced its film crystallinity which pushed in the direction of depositing better PSK crystals. The possible crosslinking between PEDOT:PSS, EDA-FG, and perovskite layer is shown in Fig. S2. At the highest concentration of the EDA-FG, the crystallinity of PSK film is reduced due to inappropriate high concentration leading to agglomeration of EDA-FG particles, which is hindered by a sulfonamide bond with PEDOT:PSS, confirmed by FTIR analysis. To approve the obtained results, the crystal size of the perovskite layer based on various HTLs is designed employing the Scherrer equation (SI), and the calculated data is listed in Table S1. More details about the Scherrer equation have been illustrated in the SI. Moreover, the attributed XRD data for GO, EDA-FG, and PEDOT:PSS is discussed in SI and revealed in Fig. 1d.

Since the resulting photocurrent is substantially influenced by the light absorbed via the HTLs on ITO, the optical characterization and related discussion of UV–vis

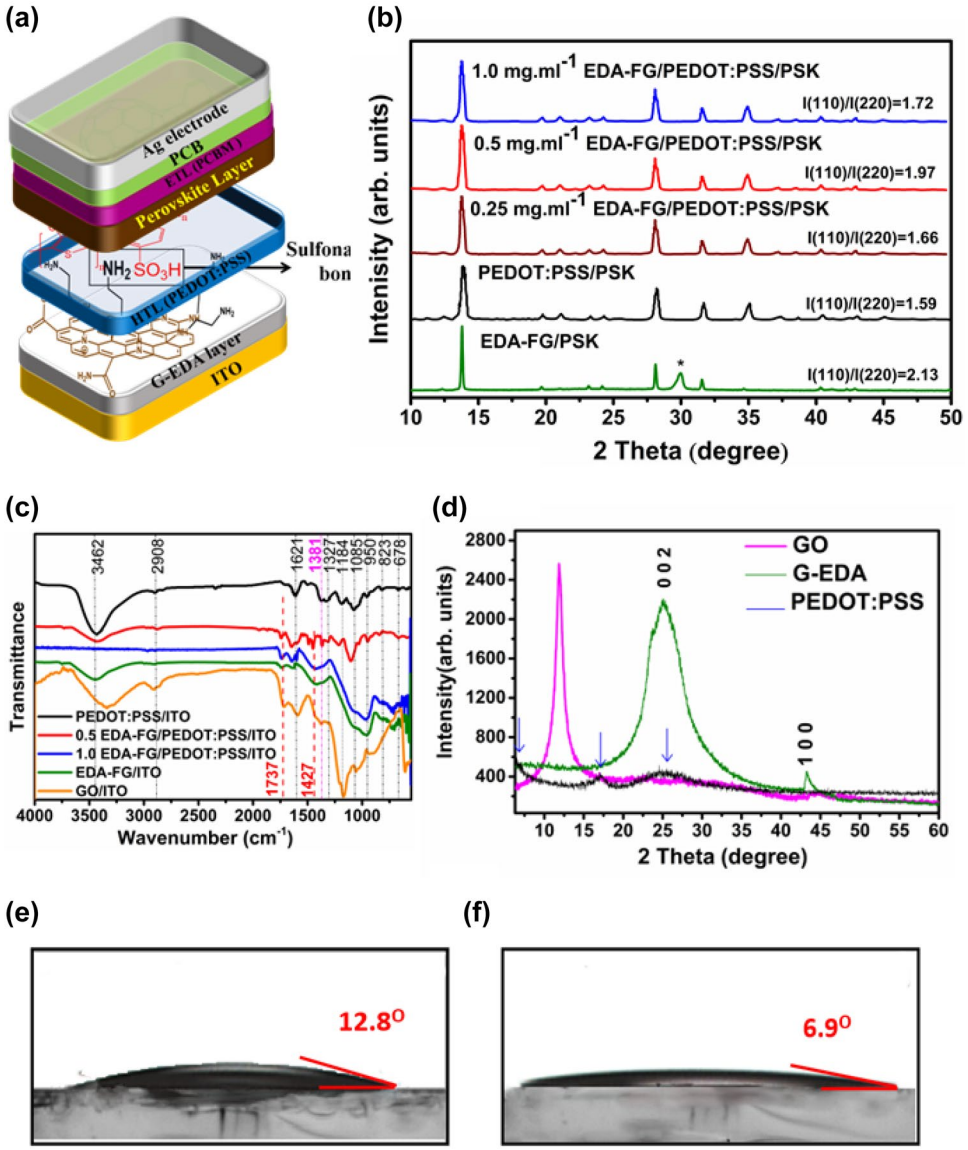

Fig. 1 **a** Schematic of possible sulfonamide bonds at bilayer EDA-FG/PEDOT:PSS interface with the PSCs inverted structure. **b** XRD spectra of $MAPbI_3$ deposited on various used HTLs. **c** FTIR of various deposited HTLs **d** XRD of GO, EDA-FG, and PEDOT:PSS. Contact angel of **e** PEDOT: PSS and **f** 0.5 GEDA mg. mL^{-1}/ PEDOT:PSS

absorption/transmission spectra, Tauc plot direct band gap, and Energies of the valence band of various deposited HTLs are presented in Fig. S3a–d. In addition, to investigate the holes' quenching and transportation abilities of the prepared pristine PEDOT:PSS and varied HTLs bilayer structure, the steady-state photoluminescence (PL) technique was utilized, and the results are illustrated in Fig. 2a. The $CH_3NH_3PbI_3$ on the top of various fabricated HTLs, including PEDOT:PSS, EDA-FG, and (0.25, 0.5, and 1.0 mg. mL^{-1}) EDA-FG/PEDOT:PSS on glass, displayed light emission at 778 nm. Compared to the PL emission of the $MAPbI_3$ based on PEDOT:PSS, the PL intensity of 0.5 EDA-FG/G-PEDOT:PSS layer decreases by about 78%. These findings reveal that holes were captured from perovskite to bilayer efficiently compared to the pristine PEDOT:PSS or EDA-FG-based devices. The mollification in the light quenching in bilayer HTL structures will result in a valance band with better matching and reduction in trap density by restraining the holes recombination at ITO/EDA-FG/PEDOT:PSS/PSK interface, which enhances the V_{OC} value [27]. Transporting of e^+ by the non-destructive C = C conjugation of EDA-FG occurs quickly through ITO/EDA-FG/PEDOT:PSS/PSK than ITO/pristine EDA-FG or PEDOT:PSS/PSK interfaces and resulting in boosts holes collection and increasing J_{SC}. The PL intensities of the fabricated layers are listed as follows: ITO/PEDOT:PSS/ PSK > ITO/EDA-FG/ PSK > ITO/0.25 EDA-FG/G-PEDOT:PSS/PSK > ITO/1.0 EDA-FG/G-PEDOT:PSS/PSK > ITO/0.5 EDA-FG/G-PEDOT:PSS/PSK. The highest concentration of EDA-FG/ PEDOT:PSS suppressed the light compared with 0.5 EDA-FG/PEDOT:PSS, which may be affected by fewer sulfonamide group formation, confirmed by FTIR characterization.

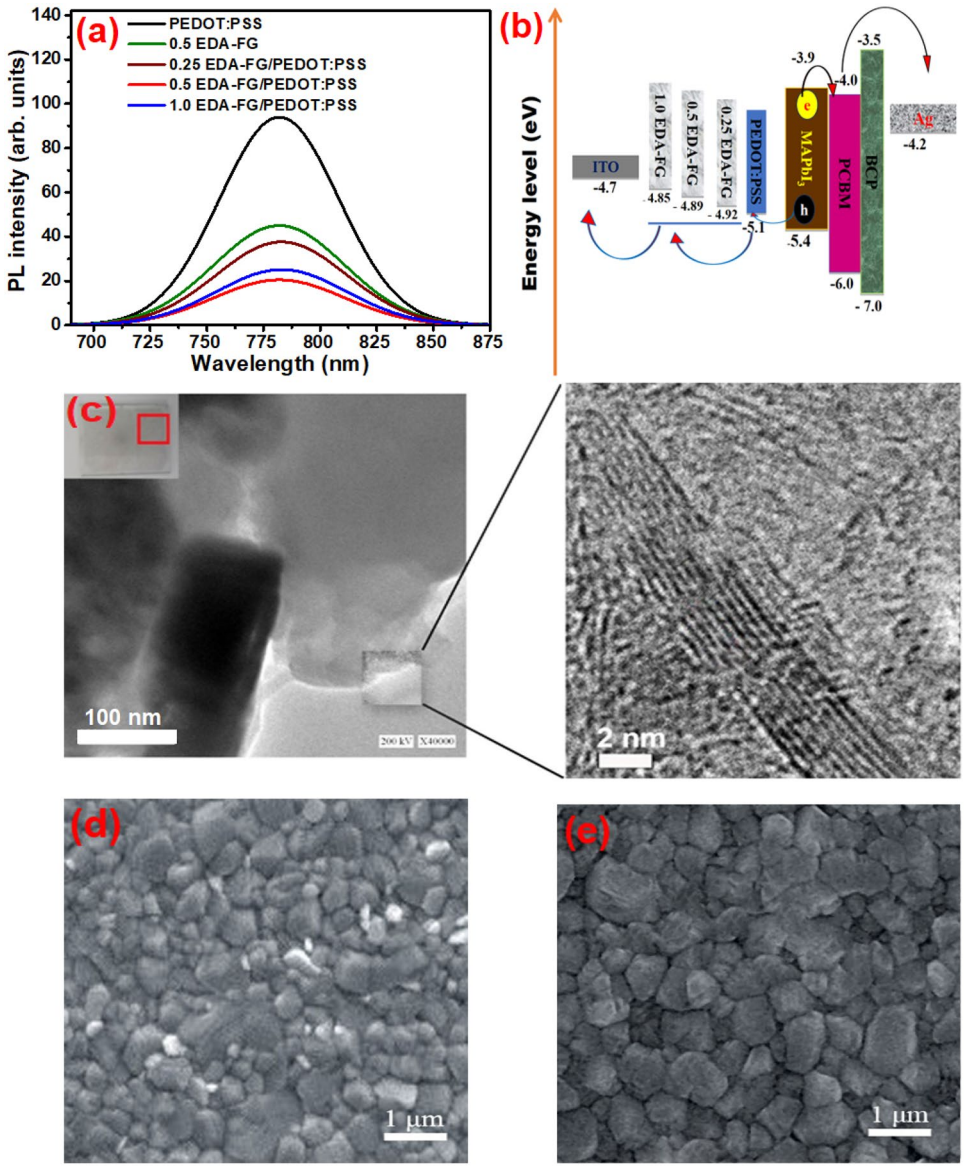

Fig. 2 **a** PL of PSK fabricated on the top of various deposited HTLs and **b** Schematic energy level diagram of different HTLs in perovskite solar cell. **c** TEM image of EDA-FG with measuring edge thickness. SEM of PSK layers on the top of **d** PEDOT:PSS, **e** 0.5 mg. mL^{-1} EDA-FG/PEDOT:PSS

The decrease in the number of sulfonamide groups in the case of 1.0 EDA-FG/PEDOT:PSS may be attributed to the aggregation of G plates at the EDA-FG highest ratio, which may strict the amine groups of EDA-FG from attaching to the sulphonic groups of PEDOT:PSS. The alignment of the energy levels for EDA-FG, PEDOT:PSS, and perovskite is seen in Fig. 2b [43].

The surface morphological features of both pristine PEDOT:PSS and 0.5 EDA-FG mg mL^{-1}/PEDOT:PSS films were examined by SEM. Significant differences in the morphology are detected, as shown in Fig. S4. The PEDOT:PSS film is smooth, whereas the film of bilayer structure, EDA-FG/PEDOT:PSS, observed that the EDA-FG fragments are scattered at the bottom of the surface of the PEDOT:PSS layer. The EDA-FG does not produce a continuous film, while its crystal size ranges from numerous hundred nanometers (nm) to tens of micrometers (µm). The EDA-FG formed only a few layers of nitrogen-doped graphitic substant over ITO with an exceptional thickness of about 2 nm, as evidenced by the TEM analysis, as depicted in Fig. 2c. The roughness of both samples on the top of ITO was detected by AFM topographic images, as seen in Fig S5a and b, where the root mean square (RMS) was 1.18 nm and 0.74 nm for pristine PEDOT:PSS and 0.5 EDA-FG/PEDOT:PSS, respectively. The lower RMS value of 0.74 nm for 0.5 EDA-FG/PEDOT:PSS compared to 1.18 nm for pristine PEDOT:PSS indicates that the former has a smoother surface. A smoother surface can lead to better contact with the active layer, less interfacial charge recombination, and higher charge collection efficiency, resulting in an improved device performance. Due to the hygroscopic properties of the polystyrene sulphonate (PSS) of the PEDOT:PSS polymer,

as emphasized by the chemical structure of the PEDOT:PSS (Fig. S6) [44], PEDOT can be dispersed in water using PSS amphipathic property; however, surrounding the PEDOT phase with a thin PSS-rich film minimizes its conductivity [45]. Therefore, overlaying the G derivatives like EDA-FG with PEDOT:PSS surface is predictable to boost the conductivity and decrease the wettability of the PEDOT:PSS layer [46, 47]. The sheet resistances of different HTLs have been measured using a four-point probe technique where it was 280 $\Omega.cm^{-2}$, 246 $\Omega.cm^{-2}$, 217 $\Omega.cm^{-2}$, and 184 $\Omega.cm^{-2}$ for pristine PEDOT:PSS, 0.25, 0.5, and 1.0 $mg.mL^{-1}$ of EDA-FG/PEDOT:PSS, respectively.

The SEM of PSK layers deposited over the PEDOT:PSS and 0.5 mg. mL^{-1} EDA-FG/PEDOT:PSS are shown in Fig. 2d and e. The crystal size of PSK over EDA-FG (0.5 mg. mL^{-1}) /PEDOT:PSS bilayer HTLs remarkably increased and became more regular compared to other HTL layers. The PSK film upward on the pristine PEDOT:PSS grew with varying crystal sizes and darkness (Fig. 2d). This fluctuation is related to PEDOT:PSS roughness and low wettability, which favors the perovskite crystal deposition in non-equal densities and distributions [47, 48]. After adding the EDA-FG under PEDOT:PSS, it worked to better arrange PSK grains via hydrogen bonds between the hydrogen atom of sulfonamide groups of deposited bilayers HTL and iodide ions (I^-) of the perovskite crystals (Fig. 2e). The 0.5 mg. mL^{-1} EDA-FG/PEDOT:PSS promotes the growth of high-quality perovskite crystals with a minor number of boundaries, which minimizes the besieged electrons and facilitates hole transport. Consequently, raising the V_{OC} and J_{SC} might enhance the associated PSC performance [49]. As clear from SEM images, the perovskite crystal is more prominent in size and reoriented in the case of the best concentration 0.5 EDA-FG under PEDOT:PSS as bilayer HTL than pristine PEDOT:PSS. The reorientation process comes from possible hydrogen bonds that may be created between sulfonamide groups of 0.5 EDA-FG/ PEDOT:PSS bilayer and perovskite crystals. This linkage rearranges perovskite crystals in a better configuration with less stress.

The *J-V* curves spectra and IPCE of the fabricated PSCs with these HTLs are demonstrated in Fig. 3a and b, respectively. All PSCs based on the HTL bilayer performed better PCE yield in reverse bias (0.25 EDA-FG/PEDOT:PSS 15.34%, 0.5 EDA-FG/PEDOT:PSS 17.66%, and 1.0 EDA-FG/PEDOT:PSS 15.67%) compared with devices based on separate PEDOT:PSS 13.71% or EDA-FG 12.87%. The J_{SC} dramatically increased from 20.32 $mA.cm^{-2}$ for the device built on PEDOT:PSS to 22.22 $mA.cm^{-2}$ based on a 0.5 EDA-FG/G-PEDOT:PSS bilayer structure. The J_{SC} value then declined to 21.30 $mA.cm^{-2}$ for 1.0 EDA-FG/PEDOT:PSS-based device. The V_{OC} slightly changes from 1.052 to 1.057 V, with the ratio of deposited EDA-FG layers raised from 0.5 to 1.0 mg/mL. Photovoltaic parameters of the champion PSCs devices are based on several HTLs, including PEDOT:PSS, EDA-FG, and (0.25, 0.5, and 1.0 mg. mL^{-1}) EDA-FG/PEDOT:PSS are listed in Table 1

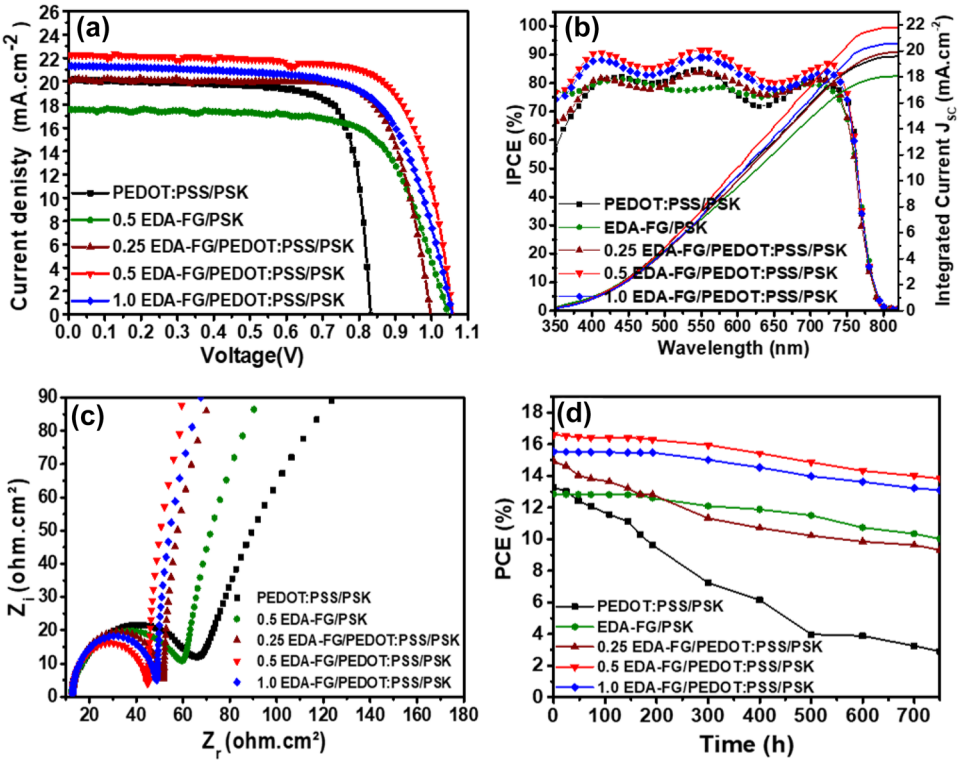

Fig. 3 **a** *J–V* curves, **b** IPCE spectra of PSCs fabricated with different HTLs. **c** EDA-FG/PEDOT:PSS in a dark condition. **c** A zoom for R_{sc} circle of perovskite solar cells fabricated with PEDOT: PSS, EDA-FG, and (0.25, 0.5, and 1.0 mg. mL^{-1}) EDA-FG/PEDOT:PSS. **d** Light soaking stability of PSCs fabricated

Table 1 Photovoltaic performance of the fabricated inverted planar PSCs with various HTLs under simulated AM 1.5 illumination (forward direction, power density 100 mW cm^{-2})

HTL	J_{SC} [mA.cm^{-2}]	V_{OC}[V]	FF	PCE [%]	Aver. PCE ± std dev. (%)	HF
PEDOT: PSS	20.33	0.83	0.79	13.33	(12.80 ± 0.53)	3.49
EDA-FG	17.59	1.05	0.70	12.92	(12.65 ± 0.27)	0.46
0.25 EDA-FG/PEDOT:PSS	20.06	1.00	0.75	15.05	(14.72 ± 0.33)	1.31
0.5 EDA-FG/PEDOT:PSS	22.22	1.05	0.74	17.26	(16.89 ± 0.37)	2.08
1.0 EDA-FG/PEDOT:PSS	21.30	1.06	0.70	15.80	(15.58 ± 0.22)	0.13

(forward direction) and Table S2 (reverse direction). From IPCE measurements (Fig. 3b), a broad spectral swap ranging from 350 to 850 nm, the integrated values of J_{SC} from IPCE spectra correspond to J_{SC} results. Every IPCE spectrum performance of devices depending on HTLs bilayer structures are similar to those fabricated with PEDOT:PSS. However, their values were higher throughout the entire wavelength than PEDOT:PSS-based devices. The integrated J_{SC} for the PEDOT:PSS, EDA-FG, 0.25 EDA-FG/PEDOT:PSS 0.5 EDA-FG/PEDOT:PSS, 1.0 EDA-FG/PEDOT:PSS, and EDA-FG based PSCs devices were 19.74 mA/cm^2, 18.01 mA/cm^2, 20.09 mA/cm^2, 21.97 mA/cm^2, and 20.63 mA/cm^2, respectively.

To further examine the diverse processes caused by inserting EDA-FG with different concentrations under PEDOT:PSS as bilayer HTLs in p-i-n type PSCs EIS is performed. EIS has been utilized as a helpful technique to inspect the process that occurs inside photovoltaic (PV) devices [50, 51]. The R_s linked to the top electrode (Ag), and ITO, R_{sc}, and R_{rec}, where sc and rec = contact resistance and recombination resistance, respectively, may be derived by fitting a matching circuit inserted in Fig. S7a. A zoom for R_{sc} circles of PSCs fabricated with PEDOT:PSS, EDA-FG, and (0.25, 0.5, and 1.0 mg. mL^{-1}) EDA-FG/PEDOT:PSS is shown in Fig. 3c. The electrical equivalent circuit (EEC) is drawn in Fig. S7b, with more detailed figures for the fitted impedance spectra for all devices are presented in Fig. S8. The EEC described the experimental data well, and the fitting electrochemical values are inserted in Table S3. The R_{sc} was due to connections or facial interactions via the perovskite film, whereas the R_{rec} was due to the recombination charge at interfaces between PSK solar cell device layers. The R_{rec} of the device increases after inserting the EDA-FG under the layer, indicating that the improved shape and more giant crystals are responsible for the reduced recombination with effective transporter relocation to the counter electrode. Smaller R_s, R_{sc}, and bigger R_{rec} were advantageous because they make it easier to separate photogenerated transporters and send them to the appropriate HTL or ETL. Refer to the SI for more details and an explanation of the EIS interpretation-based equation; refer to the supplemental file (SI). The electrical conductivity of different HTLs can be arranged as follows: ITO/EDA-FG > 1.0 EDA-FG/G-PEDOT:PSS > ITO/0.5 EDA-FG/G-PEDOT:PSS > ITO/0.25 EDA-FG/G-PEDOT:PSS ITO/PEDOT:PSS. However, the EDA-FG is the most conductive HTL, but its PCE value was the least compared with other deposited HTLs. This refers to the G derivatives deposition by the spin coating technique that cannot form a continuous film, which affects the J_{SC} and FF values (Fig. S9) [26, 47, 52, 53]. In contrast, PEDOT:PSS layer, which can be deposited in a continuous layer, showed the lowest V_{OC}. The low value of V_{OC} of the device fabricated with PEDOT:PSS as HTL is attributed to slightly compatible matching between ITO and PEDOT:PSS and low conductivity value, which reduced holes collections at the transparent conductive electrode [54]. All devices based on the bilayer HTLs structures show a synergistic effect by combining two advantages of both HTLs bilayer components where the PCE values were higher than PEDOT:PSS or EDA-FG alone.

The device with a configuration ITO/0.5 EDA-FG/G-PEDOT:PSS/PSK/PCPM/PCB/Ag appeared to have a supreme performance might be the influence of two factors: (i) collecting holes effectively through sulfonamide bands and compatibility between the various VB at the ITO/0.5 EDA-FG/PEDOT:PSS/$MAPbI_3$ interface, confirmed by WF measuring Fig. S3d, and (ii) equivalent distribution of EDA-FG on the top of ITO without pinholes as the case of 0. 5 EDA-FG or sheets agglomeration as the case of 1.0 EDA-FG, has been proved from SEM property Fig. S4b. The hysteresis behavior of the corresponding PSCs device, including forward and reverse bias, was determined using AM 1.5 G sun-lighting (1 W.cm^{-2}) via interruption duration of 50 ms, as shown in Fig. S10, where the PSCs-based devices displayed slight hysteresis because the deposited HTLs are ultrathin layers [7]. Additionally, a larger grain size of PSK crystals paves to efficient extraction of charges and suppression of charge recombination [55]. The hysteresis factor (HF) for all devices has been calculated, 1.0 mg.mL^{-1} EDA-FG/PEDOT: PSS-based device showed the lowest hysteresis may be due to this bi-film possessing the highest conductive value which facilitates the holes transfer efficiently in both scan directions (Table 1). The characteristic cross-sectional SEM of the champion device manufactured using 0.5 mg/mL EDA-FG/PEDOT:PSS bilayer structure is demonstrated in Fig. S11a. It can be noticed that EDA-FG formed only a few

layers of nitrogen-doped graphitic substant over ITO with an exceptional thickness of about 2 nm, which is previously evidenced by the TEM analysis (Fig. 2c).

The PSCs' long-term stability is an important feature of their commercialization. Figure 3d depicts the stability performances of four PSCs without encapsulation due to the storage time of over 500 h at room temperature. (55% relative humidity). Due to PEDOT:PSS's hygroscopic properties, less than 30% of the device's initial PCE value was retained after 500 h of air exposure [25]. The EDA-FG-based device was maintained at 89% from the initial measurement. The device was fabricated with a bilayer structure at a high concentration of EDA-FG (0.5 and 1.0 GEDA)/PEDOT:PSS showed low PCE loss, and the photovoltaic performance was maintained up to 88%. In contrast, the low concentration saved only 68% from the initial PSCs performance evaluation. In addition, the normalized PCE% of various devices is shown in Fig. S11b. The PSCs devices based on EDA-FG increase the stability of the corresponding device due to G derivatives. When G layers act as a substrate for PEDOT:PSS, it could mitigate the severity of the hygroscopic and wettability properties of PEDOT:PSS and the prohibition of ITO from direct contact with its PEDOT:PSS [46, 47]. The results authorized the long-term constancy of EDA-FG/PEDOT:PSS perovskite-based device compared to PEDOT:PSS, which encourages more stable and effective PSCs based on other N-FG and PEDOT:PSS as bilayer structure HTLs.

4 Conclusion

Overall, the concentration of the EDA-FG under PEDOT:PSS was optimized from 0.25, 0.5 to 1.0 mg/mL^{-1} as bilayer HTL to achieve high-performance PSCs. Then, the EDA-FG/PEDOT:PSS with different constructions were optimized by FTIR, XRD, UV, and work function (WF). Based on FTIR and XRD data, the results confer that the new linkage between EDA-FG and PEDOT:PSS leaded to rearrangement between PEDOT:PSS intermolecular, thus enhancing its film crystallinity for better PSK crystals. It was found that the valance band of EDA-FG is matched to ITO that effectively extracted and transferred the holes from the light-absorber layer to the back ITO electrode. The PL manifested that the 0.5 mg/mL EDA-FG/PEDOT as HTLs quenched the PL intensity of the $CH_3NH_3PbI_3$ layer by 78%, which is beneficial for extracting holes efficiently from perovskite compared to the pristine PEDOT:PSS-based devices, hence enhancing the V_{OC} value. EIS reveals two significant points: a decline in the charge transfer resistance (R_{CT}) and a rise in the charge's recombination at the PSCs interfaces. All PSCs based on HTL bilayer showed high-yielding PCE harvesting in reverse bias as follows: 0.25 G-EDA/PEDOT: PSS 15.34%, 0.5 G-EDA/PEDOT:PSS 17.66%, and 1.0 G-EDA/PEDOT: PSS 15.67% compared with devices based on only PEDOT:PSS 13.71%. The photovoltaics behavior estimation studies confirmed that all PSCs devices fabricated with G-EDA/PEDOT:PSS bi-layers HTL without encapsulation exhibited high stability under atmosphere conditions with light consumption for 500 h, and the PCE losses were less than 10%.

Supplementary Information The online version contains supplementary material available at https://doi.org/10.1007/s42114-023-00681-w.

Author contribution G. Al-Gamal: conceptualization, experimental, writing—original draft preparation. A. M. Elseman: writing, reviewing, and editing. M. Abdel-Shakour: Tuac and integrated current calculations. T. H. Chowdhury: experimental supervision and editing. K. I. Kabel: reviewing and supervision. A. A. Farag: electrochemical impedance spectroscopy guidance and supervision. A. M. Rabie: photoluminescent explanation and guidance. N. E. A. Abd El-Sattar: reviewing and supervision. N. Fukata: writing—reviewing and editing. A. Islam: team leader and supervision.

Funding This work is financially supported by the Japan Society for the Promotion of Science (JSPS KAKENHI) Grant No. 18H02079.

Declarations

Conflict of interest The authors declare no competing interests.

References

1. Jeon NJ, Na H, Jung EH, Yang T-Y, Lee YG, Kim G, Shin H-W, Il Seok S, Lee J, Seo J (2018) A fluorene-terminated hole-transporting material for highly efficient and stable perovskite solar cells. Nat Energy 3:682–689
2. Jeong J, Kim M, Seo J, Lu H, Ahlawat P, Mishra A, Yang Y, Hope MA, Eickemeyer FT, Kim M (2021) Pseudo-halide anion engineering for α-$FAPbI_3$ perovskite solar cells. Nature 592:381–385
3. Elseman AM, Sharmoukh W, Sajid S, Cui P, Ji J, Dou S, Wei D, Huang H, Xi W, Chu L (2018) Superior stability and efficiency over 20% perovskite solar cells achieved by a novel molecularly engineered Rutin–AgNPs/thiophene copolymer. Adv Sci 5:1800568
4. Tsiba Matondo J, Malouangou Maurice D, Chen Q, Bai L, Guli M (2021) Inorganic copper-based hole transport materials for perovskite photovoltaics: challenges in normally structured cells, advances in photovoltaic performance and device stability. Sol Energy Mater Sol Cells 224:111011
5. Sajid S, Elseman AM, Ji J, Dou S, Wei D, Huang H, Cui P, Xi W, Chu L, Li Y (2018) Computational study of ternary devices: stable, low-cost, and efficient planar perovskite solar cells. Nano-Micro Lett 10:1–11
6. Malinkiewicz O, Yella A, Lee YH, Espallargas GM, Graetzel M, Nazeeruddin MK, Bolink HJ (2014) Perovskite solar cells employing organic charge-transport layers. Nat Photonics 8:128–132
7. Hu W, Xu CY, Niu LB, Elseman AM, Wang G, Liu DB, Yao YQ, Liao LP, Zhou GD, Song QL (2019) High open-circuit voltage of 1.134 V for inverted planar perovskite solar cells with sodium citrate-doped PEDOT: PSS as a hole transport layer. ACS Appl Mater Interfaces 11:22021–22027
8. Han W, Ren G, Liu J, Li Z, Bao H, Liu C, Guo W (2020) Recent progress of inverted perovskite solar cells with a modified

PEDOT: PSS hole transport layer. ACS Appl Mater Interfaces 12:49297–49322
9. Xia Y, Dai S (2021) Review on applications of PEDOTs and PEDOT: PSS in perovskite solar cells. J Mater Sci Mater Electron 32:12746–12757
10. Ko Y, Kim Y, Lee C, Kim Y, Jun Y (2018) Investigation of hole-transporting poly (triarylamine) on aggregation and charge transport for hysteresisless scalable planar perovskite solar cells. ACS Appl Mater Interfaces 10:11633–11641
11. Liu Y, Liu Z, Lee E-C (2019) High-performance inverted perovskite solar cells using doped poly (triarylamine) as the hole transport layer. ACS Appl Energy Mater 2:1932–1942
12. Xu CY, Hu W, Wang G, Niu L, Elseman AM, Liao L, Yao Y, Xu G, Luo L, Liu D (2019) Coordinated optical matching of a texture interface made from demixing blended polymers for high-performance inverted perovskite solar cells. ACS Nano 14:196–203
13. Sajid S, Elseman AM, Wei D, Ji J, Dou S, Huang H, Cui P, Li M (2019) NiO@carbon spheres: a promising composite electrode for scalable fabrication of planar perovskite solar cells at low cost. Nano Energy 55:470–476
14. Sajid S, Elseman AM, Huang H, Ji J, Dou S, Jiang H, Liu X, Wei D, Cui P, Li M (2018) Breakthroughs in NiO_x-HTMs towards stable, low-cost and efficient perovskite solar cells. Nano Energy 51:408–424
15. Hasan AM, Raifuku I, Amin N, Ishikawa Y, Sarkar D, Sobayel K, Karim MR, Ul-Hamid A, Abdullah H, Shahiduzzaman M (2020) Air-stable perovskite photovoltaic cells with low temperature deposited NiO_x as an efficient hole-transporting material. Opt Mater Express 10:1801–1816
16. Elseman AM, Luo L, Song QL (2020) Self-doping synthesis of trivalent Ni_2O_3 as a hole transport layer for high fill factor and efficient inverted perovskite solar cells. Dalton Trans 49:14243–14250
17. Wang X, Wu J, Yang Y, Liu X, Guo Q, Song Z, Li G, Lan Z, Huang M (2019) High performance and stable perovskite solar cells using vanadic oxide as a dopant for spiro-OMeTAD. J Mater Chem A 7:13256–13264
18. Lou Y-H, Wang Z-K (2017) Aqueous-solution-processable metal oxides for high-performance organic and perovskite solar cells. Nanoscale 9:13506–13514
19. Chiang C-H, Chen C-C, Nazeeruddin MK, Wu C-G (2018) A newly developed lithium cobalt oxide super hydrophilic film for large area, thermally stable and highly efficient inverted perovskite solar cells. J Mater Chem A 6:13751–13760
20. Kaneko R, Chowdhury TH, Wu G, Kayesh ME, Kazaoui S, Sugawa K, Lee J-J, Noda T, Islam A, Otsuki J (2019) Cobalt-doped nickel oxide nanoparticles as efficient hole transport materials for low-temperature processed perovskite solar cells. Sol Energy 181:243–250
21. Elseman AM, Rashad M (2022) Influence of nitrogen atmosphere one-step heating assisted the solution processing of Kesterite Cu_2ZnSnS_4 as hole extraction on the efficacy of the inverted perovskite solar cells. Opt Mater 124:111998
22. Madhavan VE, Zimmermann I, Baloch AA, Manekkathodi A, Belaidi A, Tabet N, Nazeeruddin MK (2019) CuSCN as hole transport material with 3D/2D perovskite solar cells. ACS Appl Energy Mater 3:114–121
23. Krishna BR, Veerappan G, Bhyrappa P, Sudakar C, Ramasamy E (2022) Dual-functional inorganic CuSCN for efficient hole extraction and moisture sealing of $MAPbI_3$ perovskite solar cells. Mater Adv 3:2000–2010
24. Girish K, Vishnumurthy K, Roopa T (2022) Role of conducting polymers in enhancing the stability and performance of perovskite solar cells: a brief review. Mater Today Sustain 17:100090
25. Berhe TA, Su W-N, Chen C-H, Pan C-J, Cheng J-H, Chen H-M, Tsai M-C, Chen L-Y, Dubale AA, Hwang B-J (2016) Organometal halide perovskite solar cells: degradation and stability. Energy Environ Sci 9:323–356
26. Jokar E, Huang ZY, Narra S, Wang CY, Kattoor V, Chung CC, Diau EWG (2018) Anomalous charge-extraction behavior for graphene-oxide (GO) and reduced graphene-oxide (rGO) films as efficient p-contact layers for high-performance perovskite solar cells. Adv Energy Mater 8:1701640
27. Yin X, Zhou Y, Han J, Nan H, Tai M, Gu Y, Li J, Lin H (2018) Highly efficient inverted perovskite solar cells based on self-assembled graphene derivatives. J Mater Chem A 6:20702–20711
28. Liu J, Xue Y, Gao Y, Yu D, Durstock M, Dai L (2012) Hole and electron extraction layers based on graphene oxide derivatives for high-performance bulk heterojunction solar cells. Adv Mater 24:2228–2233
29. Ma S, Liu X, Wu Y, Tao Y, Ding Y, Cai M, Dai S, Liu X, Alsaedi A, Hayat T (2020) Efficient and flexible solar cells with improved stability through incorporation of a multifunctional small molecule at PEDOT:PSS/perovskite interface. Sol Energy Mater Sol Cells 208:110379
30. Feng S, Yang Y, Li M, Wang J, Cheng Z, Li J, Ji G, Yin G, Song F, Wang Z, Li J, Gao X (2016) High-performance perovskite solar cells engineered by an ammonia modified graphene oxide interfacial layer. ACS Appl Mater Interfaces 8:14503–14512
31. Redondo-Obispo C, Ripolles TS, Cortijo-Campos S, Alvarez AL, Climent-Pascual E, de Andrés A, Coya C (2020) Enhanced stability and efficiency in inverted perovskite solar cells through graphene doping of PEDOT: PSS hole transport layer. Mater Des 191:108587
32. Zhang X, Lin B, Wang F, Cheng Z, Shi X, Lougou BG (2020) Design of biomimetic leaf-type hierarchical nanostructure for enhancing the solar energy harvesting of ultra-thin perovskite solar cells. ES Energy Environ 10:22–33
33. Al-Gamal AG, Elseman AM, Chowdhury TH, Kabel KI, Farag AA, Rabie AM, Abd El-Sattar NEA, Islam A (2022) Promising nitrogen-doped graphene derivatives; a case study for preparations, fabrication mechanisms, and applications in perovskite solar cells. Top Curr Chem 381:6
34. Wang Y, Wang S, Chen X, Li Z, Wang J, Li T, Deng X (2018) Largely enhanced V_{OC} and stability in perovskite solar cells with modified energy match by coupled 2D interlayers. J Mater Chem A 6:4860–4867
35. Sani E, Vallejo JP, Cabaleiro D, Lugo L (2018) Functionalized graphene nanoplatelet-nanofluids for solar thermal collectors. Sol Energy Mater Sol Cells 185:205–209
36. Kim JM, Kim S, Choi S-H (2018) High-performance nip-type perovskite photodetectors employing graphene-transparent conductive electrodes N-type doped with amine group molecules. ACS Sustain Chem Eng 7:734–739
37. Kim Y, Ryu J, Park M, Kim ES, Yoo JM, Park J, Kang JH, Hong BH (2014) Vapor-phase molecular doping of graphene for high-performance transparent electrodes. ACS Nano 8:868–874
38. Hummers WS Jr, Offeman RE (1958) Preparation of graphitic oxide. J Am Chem Soc 80:1339
39. van der Pol TP, Keene ST, Saes BW, Meskers SC, Salleo A, van de Burgt Y, Janssen RA (2019) The mechanism of dedoping PEDOT: PSS by aliphatic polyamines. J Phys Chem C 123:24328–24337
40. Wang JT-W, Wang Z, Pathak S, Zhang W, deQuilettes DW, Wisnivesky-Rocca-Rivarola F, Huang J, Nayak PK, Patel JB, Yusof HAM (2016) Efficient perovskite solar cells by metal ion doping. Energy Environ Sci 9:2892–2901
41. Hu L, Sun K, Wang M, Chen W, Yang B, Fu J, Xiong Z, Li X, Tang X, Zang Z (2017) Inverted planar perovskite solar cells with a high fill factor and negligible hysteresis by the dual effect of NaCl-doped PEDOT: PSS. ACS Appl Mater Interfaces 9:43902–43909

42. Giuri A, Masi S, Colella S, Listorti A, Rizzo A, Kovtun A, Dell'Elce S, Liscio A, Esposito CC (2017) Rheological and physical characterization of PEDOT:PSS/graphene oxide nanocomposites for perovskite solar cells. Polym Eng Sci 57:546–552
43. Liu DB, Wang G, Niu LB, Chen LJ, Liu DY, Rao X, Elsemanand AM, Song QL (2019) Energy level bending of organic-inorganic halide perovskite by interfacial dipole. Phys Status Solidi (RRL) 13:1900103
44. Sun K, Zhang S, Li P, Xia Y, Zhang X, Du D, Isikgor FH, Ouyang J (2015) Review on application of PEDOTs and PEDOT:PSS in energy conversion and storage devices. J Mater Sci Mater Electron 26:4438–4462
45. Mengistie DA, Ibrahem MA, Wang P-C, Chu C-W (2014) Highly conductive PEDOT: PSS treated with formic acid for ITO-free polymer solar cells. ACS Appl Mater Interfaces 6:2292–2299
46. Lee D-Y, Na S-I, Kim S-S (2016) Graphene oxide/PEDOT:PSS composite hole transport layer for efficient and stable planar heterojunction perovskite solar cells. Nanoscale 8:1513–1522
47. Luo H, Lin X, Hou X, Pan L, Huang S, Chen X (2017) Efficient and air-stable planar perovskite solar cells formed on graphene-oxide-modified PEDOT:PSS hole transport layer. Nano-Micro Lett 9:1–11
48. Salim T, Sun S, Abe Y, Krishna A, Grimsdale AC, Lam YM (2015) Perovskite-based solar cells: impact of morphology and device architecture on device performance. J Mater Chem A 3:8943–8969
49. Zhao D, Sexton M, Park HY, Baure G, Nino JC, So F (2015) High-efficiency solution-processed planar perovskite solar cells with a polymer hole transport layer. Adv Energy Mater 5:1401855
50. Guerrero A, Garcia-Belmonte G, Mora-Sero I, Bisquert J, Kang YS, Jacobsson TJ, Correa-Baena J-P, Hagfeldt A (2016) Properties of contact and bulk impedances in hybrid lead halide perovskite solar cells including inductive loop elements. J Phys Chem C 120:8023–8032
51. Romero B, del Pozo G, Arredondo B, Martín-Martín D, Hernández-Balaguera E, González MDCL (2019) Characterization of organic and perovskite solar cells by impedance spectroscopy. Women in Renewable Energy (WiRE) 11095:110950N.
52. Zhou Z, Li X, Cai M, Xie F, Wu Y, Lan Z, Yang X, Qiang Y, Islam A, Han L (2017) Stable inverted planar perovskite solar cells with low-temperature-processed hole-transport bilayer. Adv Energy Mater 7:1700763
53. Chowdhury TH, Akhtaruzzaman M, Kayesh ME, Kaneko R, Noda T, Lee J-J, Islam A (2018) Low temperature processed inverted planar perovskite solar cells by r-GO/CuSCN hole-transport bilayer with improved stability. Sol Energy 171:652–657
54. Zuo C, Ding L (2017) Modified PEDOT layer makes a 1.52 V voc for perovskite/PCBM solar cells. Adv Energy Mater 7:1601193
55. Zhang P, Wu S, Chen Y, Li X, Sun F, Liu M, Chen Z, Li S (2022) Hysteresis-free and efficient perovskite solar cells using SnO_2 with self-assembly L-cysteine layer. Eng Sci 20:180–187